

# The detection efficiency of type Ia supernovae from the Zwicky Transient Facility: Limits on the intrinsic rate of early flux excesses

M. R. Magee<sup>1,2\*</sup>, C. Cuddy<sup>1</sup>, K. Maguire<sup>1</sup>, M. Deckers<sup>1</sup>, S. Dhawan<sup>3</sup>, C. Frohmaier<sup>4</sup>, A. A. Miller<sup>5</sup>, J. Nordin<sup>6</sup>, M. W. Coughlin<sup>7</sup>, F. Feinstein<sup>8</sup>, R. Riddle<sup>9</sup>

<sup>1</sup>*School of Physics, Trinity College Dublin, The University of Dublin, Dublin 2, Ireland*

<sup>2</sup>*Institute of Cosmology and Gravitation, University of Portsmouth, Burnaby Road, Portsmouth, PO1 3FX, UK*

<sup>3</sup>*The Oskar Klein Centre for Cosmoparticle Physics, Department of Physics, Stockholm University, SE-10691 Stockholm, Sweden*

<sup>4</sup>*School of Physics and Astronomy, University of Southampton, Southampton, SO17 1BJ, UK*

<sup>5</sup>*Center for Interdisciplinary Exploration and Research in Astrophysics and Department of Physics and Astronomy, Northwestern University, 1800 Sherman Ave, Evanston, IL 60201, USA*

<sup>6</sup>*Institute of Physics, Humboldt-Universität zu Berlin, Newton str. 15, 12489 Berlin, Germany*

<sup>7</sup>*School of Physics and Astronomy, University of Minnesota, Minneapolis, Minnesota 55455, USA*

<sup>8</sup>*Aix Marseille Univ, CNRS/IN2P3, CPPM, Marseille, France*

<sup>9</sup>*Caltech Optical Observatories, California Institute of Technology, Pasadena, CA 91125, USA*

Accepted 2022 April 09. Received 2022 April 09; in original form 2021 November 25.

## ABSTRACT

Samples of young type Ia supernovae have shown ‘early excess’ emission in a few cases. Similar excesses are predicted by some explosion and progenitor scenarios and hence can provide important clues regarding the origin of thermonuclear supernovae. They are however, only predicted to last up to the first few days following explosion. It is therefore unclear whether such scenarios are intrinsically rare or if the relatively small sample size simply reflects the difficulty in obtaining sufficiently early detections. To that end, we perform toy simulations covering a range of survey depths and cadences, and investigate the efficiency with which young type Ia supernovae are recovered. As input for our simulations, we use models that broadly cover the range of predicted luminosities. Based on our simulations, we find that in a typical three day cadence survey, only  $\sim 10\%$  of type Ia supernovae would be detected early enough to rule out the presence of an excess. A two day cadence however, should see this increase to  $\sim 15\%$ . We find comparable results from more detailed simulations of the Zwicky Transient Facility surveys. Using the recovery efficiencies from these detailed simulations, we investigate the number of young type Ia supernovae expected to be discovered assuming some fraction of the population come from scenarios producing an excess at early times. Comparing the results of our simulations to observations, we find the intrinsic fraction of type Ia supernovae with early flux excesses is  $\sim 28_{-11}^{+13}\%$ .

**Key words:** supernovae: general — radiative transfer

## 1 INTRODUCTION

The optical sky is being studied in unprecedented detail thanks to modern all-sky surveys such as the All-Sky Automated Survey for Supernovae (ASAS-SN; Shappee et al. 2014), Asteroid Terrestrial-impact Last Alert System (ATLAS; Tonry et al. 2018), and Zwicky Transient Facility (ZTF; Bellm et al. 2019a; Graham et al. 2019; Masci et al. 2019; Dekany et al. 2020). The increased cadence and area of these surveys has allowed for new and unique behaviours to be observed, including for objects that were once thought to be relatively homogeneous, such as type Ia supernovae (SNe Ia). Consensus in the literature points to thermonuclear explosions of white dwarfs in binary systems as the origin of SNe Ia (Livio & Mazzali 2018; Wang 2018; Jha et al. 2019; Soker 2019). There is little consensus however, over exactly the nature of the progenitor and explosion scenarios. In addition, observations at increasingly early times are

highlighting new and poorly understood phenomena and therefore could provide key diagnostic evidence for discriminating between different scenarios (e.g. Nugent et al. 2011; Jiang et al. 2017).

The first in-depth investigation of the progenitor system’s impact on the early light curves of SNe Ia was provided by Kasen (2010), who studied the emission generated following interaction between the SN ejecta and companion star. During the interaction, the ejecta becomes shock-heated and eventually results in UV and optical emission lasting up to a few days as the shocked ejecta expands and cools. The strength of this emission is determined by the properties of the binary system and viewing angle of the observer. Following from the arguments presented by Kasen (2010), Liu et al. (2015) investigate the range of companion interaction signatures that may be expected from binary population synthesis calculations. Related to the companion interaction scenario, Piro & Morozova (2016) investigate interaction between the SN ejecta and circumstellar material. This scenario behaves in a similar manner to that of companion interaction

\* E-mail: mrmagee.astro@gmail.com

and therefore produces similar observational signatures, namely an excess of UV and optical flux within the first few days of explosion.

Instead of interaction, an excess of flux at early times can be produced by certain explosion scenarios. The double detonation scenario involves the accretion of a helium shell on to the surface of the white dwarf (Livne 1990; Livne & Glasner 1991; Woosley & Weaver 1994). During the explosion, burning within the helium shell can lead to the production of short-lived radioactive isotopes, such as  $^{56}\text{Ni}$ ,  $^{52}\text{Fe}$ , and  $^{48}\text{Cr}$ . The decay of these isotopes in the outer ejecta drives the early emission for the first few days following explosion (Noebauer et al. 2017; Jiang et al. 2017; Polin et al. 2019; Magee et al. 2021). Depending on the mass and composition of the helium shell, a wide variety of behaviours at early times can be produced (Maeda et al. 2018; Magee et al. 2021). Similarly, shells or clumps of  $^{56}\text{Ni}$  present in the outer ejecta could also lead to excess emission at early times, before the primary  $^{56}\text{Ni}$  mass in the inner ejecta powers the main rise of the light curve (Dimitriadis et al. 2019; Magee & Maguire 2020). Such clumps could arise from deflagrations in Chandrasekhar-mass white dwarfs (Seitenzahl et al. 2016)

Observations of SNe Ia within these crucial early phases are becoming increasingly routine and, as such, dedicated searches for the signatures of these scenarios have been undertaken. Cao et al. (2015) present observations of iPTF14atg, the first SN Ia discovered with a prominent UV flash at early times. The origin of this early excess is contentious, with arguments presented for and against interaction scenarios (Cao et al. 2015; Liu et al. 2015; Kromer et al. 2016). Subsequent in-depth analyses for the few SNe Ia with clear early excesses have demonstrated the wide variety of early emission behaviours observed (Jiang et al. 2017; Hosseinzadeh et al. 2017; De et al. 2019; Dimitriadis et al. 2019; Shappee et al. 2019; Miller et al. 2020; Ni et al. 2022). It is likely that more than one scenario is required to explain the full diversity observed (Magee et al. 2021).

While a handful of SNe Ia with early excesses are now known, it is not clear whether the scenarios producing such excesses are intrinsically rare or if we simply lack sufficient coverage at early times to detect them. In this work, we perform a direct investigation of the efficiency with which early excesses in the light curves of SNe Ia are recovered. We further use this analysis to place limits on the rate of objects with such excesses. In Sect. 2 we discuss the different model scenarios used as part of this work. Section 3 provides a description of *simsurvey*<sup>1</sup> (Feindt et al. 2019), which is used to perform our simulations of surveys with various different observing strategies. In Sect. 4 we present the results of a series of toy simulations that directly explore the impact of cadence and observing depth on the recovery efficiency of young SNe Ia. Section 5 presents the results of simulations based on observing logs from ZTF. Section 6 uses our simulations of the actual ZTF observing strategy to calculate the rate of SNe Ia from ZTF and places limits on the intrinsic fraction of SNe Ia that may produce early flux excesses. We discuss our results in Sect. 7. Finally, in Sect. 8, we present our conclusions.

## 2 MODEL SN IA LIGHT CURVES

Here, we outline the different models used as part of our survey simulations. These models were chosen due to the great diversity in their early time behaviours and general similarities to observed flux excesses, which will allow us to place meaningful constraints on the expected rates of early time flux excesses in SNe Ia.

<sup>1</sup> <https://simsurvey.readthedocs.io/en/latest/>

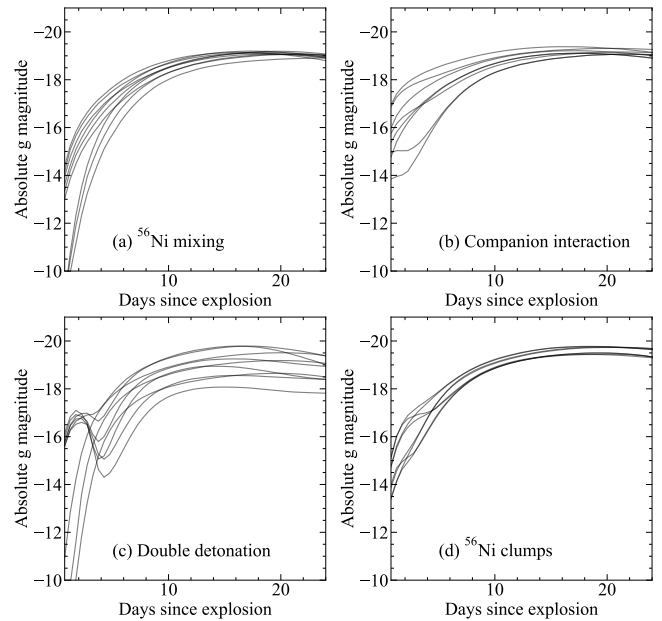


**Figure 1.** Representative examples of light curves for the four model scenarios considered in this work.

### 2.1 Model scenarios

Each model is based on one of the following four scenarios:  $^{56}\text{Ni}$  mixing, companion interaction, double detonation, and  $^{56}\text{Ni}$  clumps. The free parameters for each scenario are given in Table 1. Here we provide a brief overview of each scenario. References for more detailed information are given in Table 1. A selection of representative light curves are also shown in Fig. 1.

All model light curves were calculated using *TURTLES* (Magee et al. 2018; Magee & Maguire 2020; Magee et al. 2021). Briefly, *TURTLES* is a one-dimensional Monte-Carlo radiative transfer code for modelling thermonuclear SNe. The structure of the ejecta is a free parameter in the simulations and therefore *TURTLES* can be used to explore a multitude of different explosion scenarios. During each *TURTLES* simulation, *TARDIS* (Kerzendorf & Sim 2014) is used to calculate opacities throughout the model. One of the limitations of *TURTLES* is the assumption of local thermodynamic equilibrium (LTE) and therefore simulations are stopped 30 days after explosion. We note however that, by comparing spectra calculated using LTE and non-LTE ionisation approximations, Shen et al. (2021) have recently demonstrated that the differences between the two ionisation treatments are negligible until approximately two weeks after maximum light. Therefore the assumption of LTE should have a minimal impact on the light curves of our models. Nevertheless, the model light curves used in this work do not cover the full decline after maximum light. While this study primarily focuses on the recovery efficiency during the earliest phases, and not around maximum light, we also assess the impact of this limitation. We calculate additional survey simulations using SN Ia templates from Hsiao et al. (2007), which represents the mean evolution of the SN Ia spectral energy distribution (SED), based on the compilation of a large sample of observed spectra. This is discussed further in Sect 5.1.

For the first scenario considered here,  $^{56}\text{Ni}$  mixing in Chandrasekhar-mass explosions, we use the models provided by Magee et al. (2018, 2020). These models have been previously shown to broadly reproduce the light curve shapes and colours of multiple SNe Ia without flux excesses at early times (Magee et al. 2020; Deck-

ers et al. 2022). They may therefore be considered as representative examples of relatively ‘normal’ SNe Ia and will serve as useful reference points in comparison to models that do produce flux excesses. Each model is characterised by the  $^{56}\text{Ni}$  mass,  $^{56}\text{Ni}$  distribution, and density profile. The shape of the density profile is determined by the kinetic energy, while the  $^{56}\text{Ni}$  distribution is given using the following functional form for the  $^{56}\text{Ni}$  mass fraction at mass coordinate  $m$ :

$$^{56}\text{Ni}(m) = \frac{1}{\exp(s[m - M_{\text{Ni}}]/M_{\odot}) + 1}, \quad (1)$$

where  $M_{\text{Ni}}$  is the total  $^{56}\text{Ni}$  mass in  $M_{\odot}$  and  $s$  is the scaling parameter, controlling how quickly the ejecta transitions from  $^{56}\text{Ni}$ -rich to  $^{56}\text{Ni}$ -poor. Both the density profile and  $^{56}\text{Ni}$  distribution have a significant impact on the early light curve. Magee et al. (2020) showed how the  $^{56}\text{Ni}$  distribution of SNe Ia can vary greatly, but the vast majority of SNe Ia considered in their sample were reasonably well matched by intermediate to extended  $^{56}\text{Ni}$  distributions. None of the SNe Ia considered were reproduced by models in which there is a sharp transition between  $^{56}\text{Ni}$ -rich and  $^{56}\text{Ni}$ -poor regions of the ejecta. In the parameterisation used by Magee et al. (2020), these models are given by large  $s$  values (e.g.  $s = 21, 100$ ), while smaller  $s$  values indicate a more extended distribution (e.g.  $s = 3, 4.4$ ), with  $^{56}\text{Ni}$  present throughout the entire ejecta. Given the disagreement between the highly stratified models and observations of SNe Ia, we do not consider such models as part of our simulations here. For the present work, we take the models with  $0.5 M_{\odot}$  of  $^{56}\text{Ni}$  used by Deckers et al. (2022), which are consistent with the peak luminosities of SNe Ia from ZTF (Deckers et al. 2022) and other studies (e.g. Scalzo et al. 2014). In this case, for  $s = 3$ , the  $^{56}\text{Ni}$  fraction in the outermost ejecta is  $\sim 0.06$ , while for  $s = 9.7$  it is approximately two orders of magnitude lower (see also fig. 1 of Magee et al. 2020).

In addition to  $^{56}\text{Ni}$  mixing, we also consider the impact of interaction with a companion red-giant or main sequence star for Chandrasekhar-mass explosions. For this purpose, we take a subset of the previously described  $^{56}\text{Ni}$  mixing models (see Table 1) as the base models. For each of these models, we add the flux produced by companion interaction. We use the analytical expressions presented by Kasen (2010) (equations 22 and 25) to calculate the black-body emission for a given binary separation ( $a$ ). We note that a few simplifying assumptions are made for these analytical expressions, particularly with regards to the shape of the density profile and the opacity. Nevertheless, they are still useful as an indication of the luminosity expected, are generally consistent with more detailed numerical simulations (Kasen 2010), and have been used in numerous studies to search for signs of interaction (e.g. Hayden et al. 2010; Brown et al. 2012; Cao et al. 2015; Olling et al. 2015; Miller et al. 2020). For each underlying  $^{56}\text{Ni}$  mixing model, following from Kasen (2010), we consider four types of companions: a  $\sim 1 M_{\odot}$  red giant ( $a = 2 \times 10^{13}$  cm), a  $\sim 6 M_{\odot}$  main sequence star ( $a = 2 \times 10^{12}$  cm), a  $\sim 2 M_{\odot}$  main sequence star ( $a = 5 \times 10^{11}$  cm), and a  $\sim 1 M_{\odot}$  main sequence star ( $a = 3 \times 10^{11}$  cm). In addition, Brown et al. (2012) present an analytical expression for the variation of the black-body emission as a function of viewing angle (see their equation 3). For a given underlying  $^{56}\text{Ni}$  mixing model and companion, we calculate the emission for four viewing angles:  $0^{\circ}$ ,  $45^{\circ}$ ,  $90^{\circ}$ , and  $135^{\circ}$ . Models observed at  $0^{\circ}$  are viewed directly along the line of sight of the shocked region and therefore will show the strongest signs of interaction. Those viewed at  $180^{\circ}$  however, would not show signs of interaction and therefore are the same as models without an additional black-body component.

Despite arising from a different mechanism, the early excesses

produced by double detonation explosions may be qualitatively similar to those of companion interaction (Maeda et al. 2018). In double detonation models, the observables are strongly affected by the post-explosion composition of the helium shell (e.g. Kromer et al. 2010). For those models containing large amounts of iron-group elements and short-lived radioactive isotopes (in the form of  $^{56}\text{Ni}$ ,  $^{52}\text{Fe}$ , or  $^{48}\text{Cr}$ ) an excess of flux is produced at early times (Jiang et al. 2017; Noebauer et al. 2017), while observables around maximum light are typically characterised by red colours and spectra that are inconsistent with normal SNe Ia (Höflich & Khokhlov 1996; Höflich et al. 1996; Kromer et al. 2010; Woosley & Kasen 2011). Magee et al. (2021) present a series of sub-Chandrasekhar mass double detonation models exploring the impact of the helium shell mass and composition on the synthetic observables. For this work, we take those models from Magee et al. (2021) with  $^{56}\text{Ni}$ ,  $^{52}\text{Fe}$ , or  $^{48}\text{Cr}$  dominated shells. In all cases, a flux excess is produced at early times, the strength and duration of which depends on both the mass and composition of the helium shell. Conversely, models that do not contain iron-group elements in the shell, but are instead dominated by intermediate-mass elements (such as  $^{32}\text{S}$ ), do not produce an excess. Instead, these models are generally consistent with normal SNe Ia (Kromer et al. 2010; Townsley et al. 2019; Magee et al. 2021). We therefore also include models from Magee et al. (2021) with  $^{32}\text{S}$ -dominated shells, as further examples of normal SNe Ia without flux excesses.

Our final scenario,  $^{56}\text{Ni}$  clumps in the outer ejecta following Chandrasekhar-mass explosions, is qualitatively similar to double detonations in which the post-explosion helium shell is dominated by  $^{56}\text{Ni}$ . A clump of  $^{56}\text{Ni}$  in the outer ejecta was suggested as one possible explanation for the flux excess observed in SN 2018oh (Dimitriadis et al. 2019). Following from this, Magee & Maguire (2020) investigate  $^{56}\text{Ni}$  clumps and their impact on light curves and spectra up to maximum light. Magee & Maguire (2020) take fiducial models from Magee et al. (2020) that reproduce the light curves of SNe 2017cbv and 2018oh around maximum light, but ignore the early flux excesses. To match the shape of the flux excesses, Magee & Maguire (2020) add a clump of  $^{56}\text{Ni}$  into the outer ejecta of each fiducial model and calculate light curves and spectra. For each fiducial model, they test the range of clump masses and distributions required to match the early observations (see fig. 2 of Magee & Maguire 2020). For our survey simulations, we include all models with  $^{56}\text{Ni}$  clumps from Magee & Maguire (2020) and extend this to include additional smaller mass  $^{56}\text{Ni}$  clumps calculated as part of this work. Furthermore, Magee & Maguire (2020) compare their clump models to those with different  $^{56}\text{Ni}$  distributions. We also include these models, and the fiducial SNe 2017cbv and 2018oh models without excesses, in our survey simulations. Again, these models represent normal SNe Ia that do not produce flux excesses at early times.

Across each of these four scenarios, a total of 313 models are used in this work. This includes 31  $^{56}\text{Ni}$  mixing models, 96 companion interaction models, 168 double detonation models, and 18  $^{56}\text{Ni}$  clump models. In Fig. 2, we show the distribution of absolute  $g$ -band magnitudes at 1 d after explosion for each of our models. While these models cover a range of light curve behaviours, the full evolution of each underlying model itself is not overly important. The most relevant aspect for this work is the behaviour of each model within the first few days after explosion. Again, the models included as part of our simulations were chosen due to the broad range of early light curves predicted.

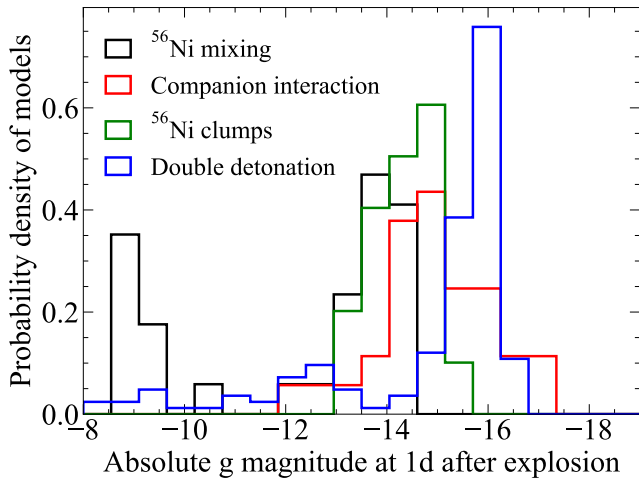


**Figure 2.** Distributions of absolute g-band magnitudes for input models at 1 d after explosion.

## 2.2 Early excess classification

The models included in our survey simulations show significant variation in their early light curves. To aid in the interpretation of our results, it is useful to classify each model based on this behaviour. We therefore present three classifications: no excess, bump, or shoulder.

Our first classification, no excess, is shown in Fig. 3(a). Of our 313 models, 70 would not be expected to contain an excess. This includes all 31  $^{56}\text{Ni}$  mixing models (as demonstrated by Magee et al. 2020, a monotonically decreasing  $^{56}\text{Ni}$  distribution towards the outer ejecta will not produce an early excess) and the 39 double detonation models with  $^{32}\text{S}$ -dominated shells. The latter are clearly seen in Fig. 1(c).

For the remaining 243 models, some show an early peak followed by a sharp decline (Fig. 3(b)), while others exhibit a quick rise initially followed by a small plateau before joining the main rise of the light curve (Fig. 3(c)). These two examples demonstrate the need for classification, as models with an early decline may typically be fainter at early times than those with a plateau. This could make them generally more difficult to detect early. To separate these cases, we define models as containing ‘bumps’ if they show a decline of at least 0.1 mag within the first five days after explosion. The choice of 0.1 mag is arbitrary, but does not have an effect on our results. This classification scheme is simply made to better understand our results, but does not impact our survey simulations. Models that do contain an excess and do not decline by 0.1 mag are classified as having ‘shoulders’. We also note that this classification scheme is based on models (i.e. *a priori* knowledge of the underlying light curve) and cannot necessarily be easily transferred to observations. In particular, discriminating between a broad light curve, a bump, and a shoulder in real SNe Ia may be difficult due to limited data and incomplete sampling (e.g. a typical 3 d cadence). Representative examples of our three early light curve classifications are given in Fig. 3.

## 3 SIMSURVEY

We use `simsurvey` (Feindt et al. 2019) throughout our analysis. `simsurvey` is a publicly available python package for simulating arbitrary survey schedules and/or transients. It has also been successfully applied to investigating the rates of SNe and kilonovae (Feindt et al. 2019; De et al. 2020; Kasliwal et al. 2020; Almualla

**Table 1.** Model properties

Free parameter	Values studied
$^{56}\text{Ni}$ mixing <sup>1</sup>	
Kinetic energy ( $10^{51}$ erg)	0.50, 0.60, 0.65, 0.78, 1.10, 1.40, 1.68, 1.81, 2.18
$^{56}\text{Ni}$ mass ( $M_{\odot}$ )	0.5
$^{56}\text{Ni}$ distribution, s	3, 4.4, 9.7
Companion interaction <sup>1,2,3</sup>	
Kinetic energy ( $10^{51}$ erg)	0.65, 1.10, 1.68
$^{56}\text{Ni}$ mass ( $M_{\odot}$ )	0.5
$^{56}\text{Ni}$ distribution, s	3, 9.7
Companion separation, $a$ (cm)	$2 \times 10^{13}$ , $2 \times 10^{12}$ , $5 \times 10^{11}$ , $3 \times 10^{13}$
Viewing angle	$0^{\circ}$ , $45^{\circ}$ , $90^{\circ}$ , $135^{\circ}$
Double detonation <sup>4</sup>	
Core mass ( $M_{\odot}$ )	0.9, 1.0, 1.1, 1.2
Helium shell mass ( $M_{\odot}$ )	0.01, 0.04, 0.07, 0.10
Fraction of shell burned	0.2, 0.5, 0.8
Helium shell composition	$^{32}\text{S}$ , $^{48}\text{Cr}$ , $^{52}\text{Fe}$ , $^{56}\text{Ni}$
$^{56}\text{Ni}$ clump <sup>5</sup>	
Core $^{56}\text{Ni}$ mass ( $M_{\odot}$ )	0.6, 0.8
Kinetic energy ( $10^{51}$ erg)	1.68, 1.10
Core $^{56}\text{Ni}$ distribution, s	4.4, 9.7
$^{56}\text{Ni}$ clump mass ( $M_{\odot}$ )	0.000, 0.005, 0.010, 0.020, 0.030, 0.040
$^{56}\text{Ni}$ clump width ( $M_{\odot}$ )	0.06, 0.18

Further details for each model scenario are provided in the following references: <sup>1</sup> Magee et al. (2020); <sup>2</sup> Kasen (2010); <sup>3</sup> Brown et al. (2012); <sup>4</sup> Magee et al. (2021); <sup>5</sup> Magee & Maguire (2020)

et al. 2021; Andreoni et al. 2021; Sagués Carracedo et al. 2021). For each simulation, a survey plan and transient model(s) are required.

The survey plan is given as a list of pointings for each observation and includes the time of observation, right ascension and declination, filter, and limiting magnitude. To demonstrate the impact of survey strategy on the early excess recovery efficiency, we explore a series of toy survey plans for which we arbitrarily select a fixed cadence of 0.2 d to 7.0 d and a uniform  $5\sigma$  limiting magnitude of 18 – 25 in both the  $g$ - and  $r$ -bands. The results of our toy simulations are given in Sect. 4.

In addition, we simulate four realistic survey plans based on observing logs from ZTF: ZTF I, ZTF I public, ZTF II public, and high cadence. By using real observing logs from ZTF, these simulations naturally include time lost due to weather and variations in image quality and our predictions can be directly compared with observations. The results of these simulations are presented in Sect. 5. Observing time for ZTF is split across multiple different public and partnership surveys (Bellm et al. 2019b). Our ‘ZTF I’ survey plan is based on approximately the first year of ZTF operations (March 2018 – December 2018). During this time, almost 40% of the total observing time was allocated to a public 3 d cadence survey of the northern sky. A large fraction of the partnership observing time was allocated to an extragalactic high cadence survey, with six visits every night for selected fields. Further details of the surveys constituting ZTF observing time are given in Bellm et al. (2019b). In ZTF I we include all of the public and partnership observations (but exclude proprietary

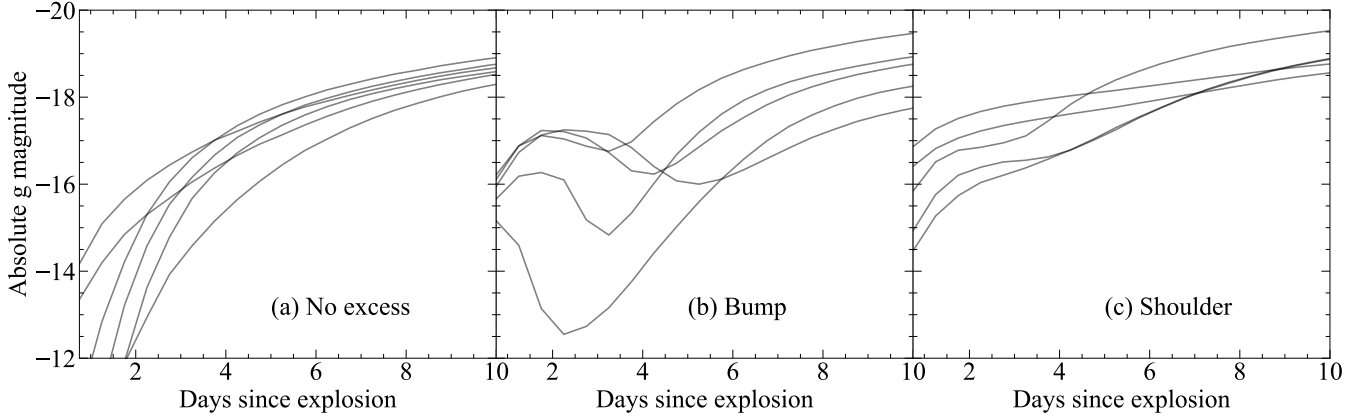


**Figure 3.** Representative examples of early flux excess classifications. Models are classified as having bumps if they show a decline of  $>0.1$  mag after an initial peak. Otherwise models with early excesses are classified as having shoulders.

Caltech time). The ‘ZTF I public’ survey plan is formed from a subset of the ZTF I plan and includes only observations from the public survey. Since the end of 2020, the cadence of the ZTF public survey has increased to 2 d. Therefore ‘ZTF II public’ includes the first six months of observations from this higher cadence public survey. Finally, the ‘high cadence’ survey plan is also formed from a subset of the ZTF I survey plan. Here, we select the most well-observed fields and include all observations from the public and partnership surveys. For these fields, the typical cadence is significantly higher at 0.5 d. Details of each survey strategy are given in Table 2, including the area, length of time covered by our simulations, and median cadence per field.

In addition to the survey plan, we also require a transient generator, which produces the observed light curves based on an underlying model SED, extinction, and redshift. As the relative rates of SNe Ia with early excesses are unknown, in each survey simulation we assume that only one type of transient will occur (using the models described in Sect. 2). For our toy simulations we focus on a specific subset of the models, which is discussed in Sect. 4. For our more realistic ZTF simulations, we simulate all of the 313 models for each survey plan. Transient coordinates are randomly selected from the area of each survey plan. We include Milky Way extinction, based on the galactic extinction map from Schlegel et al. (1998), and host extinction following from Feindt et al. (2019), where  $R_V = 2$  and  $E(B - V)$  is randomly selected from an exponential distribution with a rate of  $\lambda = 0.11$ . The time of explosion for each transient is randomly sampled from the duration of each survey plan. Finally, transients are injected up to redshift  $z = 0.1$ , beyond which the recovery efficiency decreases significantly. In each simulation, we generate 100 000 transients and calculate the fraction recovered. This results in approximately 31 million transients simulated per ZTF survey plan.

Throughout this work, we use ‘detections’ to refer to simulated observations in which the flux is greater than the flux uncertainty and inconsistent with zero, for example  $5\sigma$  detections. We use ‘recovered’ to refer to any transient that has at least two  $5\sigma$  detections at any point in the light curve across all bands or meets the stricter criteria described in later sections (e.g. Sect. 6).

**Table 2.** Survey plans used for ZTF simulations

Survey plan	Area	Duration	Cadence (days)
ZTF I	24 000 deg <sup>2</sup>	Mar. 2018 – Dec. 2018	3.0
ZTF I public	24 000 deg <sup>2</sup>	Mar. 2018 – Dec. 2018	3.0
ZTF II public	24 000 deg <sup>2</sup>	Dec. 2020 – May 2021	2.0
High cadence	110 deg <sup>2</sup>	Apr. 2018 – July 2018	0.5

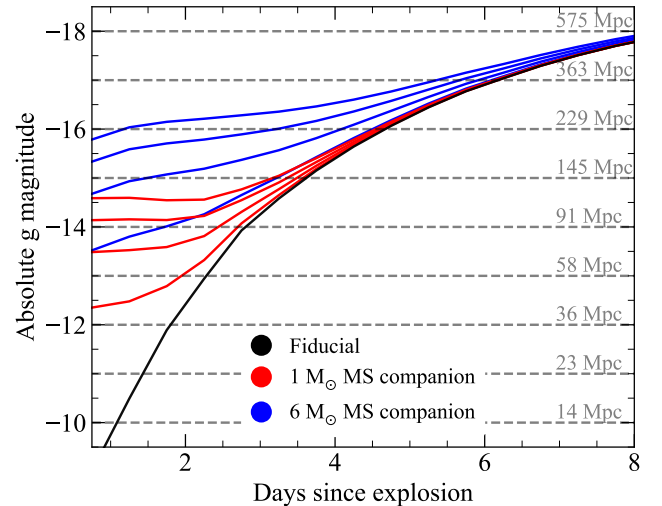


**Figure 4.** Input model light curves for our fiducial model and models to which companion interaction has been added. For each companion, we show four different viewing angles, as given in Table 1. As the viewing angle increases, the companion interaction signature decreases. Dashed horizontal lines and values in grey give the maximum luminosity distance at which each absolute magnitude is visible, assuming a  $5\sigma$  limiting magnitude of  $m_g = 20.8$ .

## 4 TOY SIMULATIONS

We first demonstrate the importance of survey depth and cadence in the recovery efficiency of young SNe Ia using a series of toy simulations. We also show how changes in the early luminosity (for example the presence of an excess) affect these recovery efficiencies. For these toy simulations, we assume uniform cadence and survey depth for the  $g$ - and  $r$ -bands. Although unrealistic, this allows us

to directly demonstrate the improvements that may be expected for higher cadence and/or fainter observations.

As input for our toy simulations, we take a fiducial model without an early excess and compare the early recovery efficiency to models with an excess. As our fiducial model without an excess we select one of our mixing models with an intermediate  $^{56}\text{Ni}$  distribution. For our excess comparisons, we select the models to which the companion interaction signature has been added to the fiducial model. For these purposes, we investigate two types of companions, a  $1 M_{\odot}$  main sequence star and a  $6 M_{\odot}$  main sequence star. For both types of companions, we also include the full range of viewing angles given in Table 1. The input model light curves are shown in Fig. 4. In Fig. 4, we also show the maximum redshift at which various absolute magnitudes would be visible, assuming a  $5\sigma$  limiting magnitude of  $m_g = 20.8$ . From Fig. 4, it is clear that our fiducial model could only be observed at  $\sim 1$  d after explosion if it was extremely nearby ( $\lesssim 15$  Mpc). The signatures of companion interaction with a  $1 M_{\odot}$  MS companion star increase the early luminosity by 2–4 mag, depending on the viewing angle. As such, the models should be detectable at 1 d after explosion out to 40–120 Mpc. Likewise, interaction with a  $6 M_{\odot}$  MS companion increases the early luminosity by 3–5 mag and hence should be detectable out to 80–230 Mpc. Early excesses that increase the luminosity by a factor of  $X$  should similarly increase the observable distance by a factor of  $\sqrt{X}$ .

Figure 5 shows the results of our toy simulations and gives the percentage of injected models that are recovered within 1 and 3 d of explosion for various combinations of survey depth and cadence. Up to 1 d after explosion, our fiducial model is not recovered for almost all toy surveys. As shown by Fig. 4, this results from the faint luminosity at this time, which will only be observable for the most nearby cases. With a survey depth of  $m \sim 25$ , the first  $\sim 1$  d of our fiducial model would be observable out to  $\sim 100$  Mpc, however a high cadence is also required to actually observe these fleeting moments. Even in these cases  $\lesssim 1\%$  of our injected fiducial models are recovered within 1 d of explosion. Increasing the early luminosity by  $\sim 3$  mag results in  $\sim 0.05\%$  of SNe Ia being detected within 1 d of explosion for a typical depth and cadence of 21 and 3 d. Further increasing the early luminosity by an additional  $\sim 2.5$  mag results in  $\sim 1.2\%$  of the injected models being recovered within 1 d of explosion. As shown by Fig. 4, a typical survey depth of  $\sim 21$  would be sensitive to these SNe up to a redshift of  $\sim 220$  Mpc. By 3 d after explosion, our fiducial model would still only be visible out to  $\sim 100$  Mpc (see Fig. 4). At this time,  $\sim 0.15\%$  of our injected fiducial models have been recovered for a typical depth and cadence of 21 and 3 d. In comparison, 0.5–8% of the excess models have been recovered. Despite being a similar magnitude to the fiducial model at this time, the excess model shown in Fig. 5 was significantly brighter at earlier times and hence more of the injected models have been recovered.

From Fig. 5 the impact of cadence is less significant than survey depth on determining the number of young SNe Ia discovered. Moving from a three to two day cadence for the same survey depth likewise results in  $\sim 50\%$  more SNe Ia discovered within approximately 1 d of explosion. We note however that a reasonably high cadence would be necessary to, for example, resolve the shape of the early excess and provide tighter constraints on pre-explosion non-detections. In Sect. 5, we compare the results of our toy simulations to the more detailed simulations of ZTF. In addition, these toy simulations assume uniform cadence for both bands and therefore may not necessarily be applicable to surveys with more complicated scheduling. For example, the upcoming Vera C. Rubin Observatory’s Legacy Survey of Space & Time (LSST; Ivezic et al. 2008; LSST Science Collaboration et al. 2009) is expected to reach a single-visit depth of  $\sim 24$  in the  $g$ -

and  $r$ -bands. Based on Fig. 5, one may naively expect that  $\gtrsim 10\%$  of all SNe Ia up to  $z = 0.1$  would be discovered by LSST early enough to determine whether an excess is present. The baseline `minion_1016` observing strategy has a typical inter-night gap of  $\sim 3$  d across all bands, while the gap for same-band observations could be  $\gtrsim 15$  d. Since excesses are predicted to be prominent in blue bands and not redder bands, this could result in cases where the SN excess is simply below the detection threshold in redder bands even though the field was observed. Hence, the recovery fractions given in Fig. 5 would be overly optimistic. The proposed `altsched` observing strategy does have a typical inter-gap for  $r$ -band observations of  $\sim 3$  d, however the gap between  $g$ -band observations remains large. We therefore caution against over interpretation of Fig. 5 for surveys with complicated scheduling requirements. More detailed simulations are necessary to fully understand the effect of these on the recovery of young SNe Ia.

## 5 ZTF SIMULATIONS

### 5.1 General recovery efficiency

Here we briefly discuss the overall recovery efficiency of ZTF. In Fig. 6, we show a sky-map of the recovery fraction for our ZTF I survey plan, which includes all of the 313 models discussed in Sect. 2. As demonstrated by Fig. 6, our ZTF I (and indeed ZTF I and II public) survey plan include fields around the galactic plane, which have significantly smaller recovery fractions than other sky positions. We exclude those transients injected close to the galactic plane ( $|b| < 15^\circ$ ) from our recovery statistics.

We find the mean recovery fraction for our ZTF I survey plan is  $\sim 56\%$ . This accounts for transients that were lost due to occurring in fields not observed when the SN was active and those falling into field/chip gaps, in addition to those that simply were not bright enough to pass the detection criteria. For the ZTF I and II public survey plans, we find similar recovery efficiencies. Unsurprisingly, the high cadence survey plan has the highest recovery efficiency ( $\sim 90\%$ ) as it is focused on a much smaller area and time. Figure 4 demonstrates that ZTF should be sensitive to SNe Ia across the entire redshift range of our simulations ( $z \leq 0.1$ ) for a few weeks surrounding maximum light. As such, we find only minor decreases in the recovery efficiencies at higher redshift compared to low redshift (4–8%).

As previously mentioned, the light curves used in these simulations extend up to approximately a few days after maximum light. The overall recovery fractions discussed thus far for our ZTF simulations will therefore typically be lower than simulations that include the full light curve evolution. To assess the impact of this limitation, we perform additional simulations using each of our survey plans and the Hsiao et al. (2007) spectroscopic template. We use two light curves based on this template; the first extends up to 40 d post-maximum (full), and the second extends up to only 5 d post-maximum (early). When using only the early Hsiao et al. (2007) template light curve, we find recovery efficiencies comparable to our other ZTF simulations. When considering the full light curve however, there is a  $\lesssim 13\%$  increase in the overall fraction of transients recovered across the redshift range simulated for all of our survey plans. The more limited light curve coverage for the models used in this work therefore has only a minor impact on our ability to recover transients, but the overall recovery efficiencies quoted here should be considered as lower limits with an absolute uncertainty of  $\sim 13\%$ . This does not impact the recovery efficiencies for young SNe Ia, which are the main focus of this work.

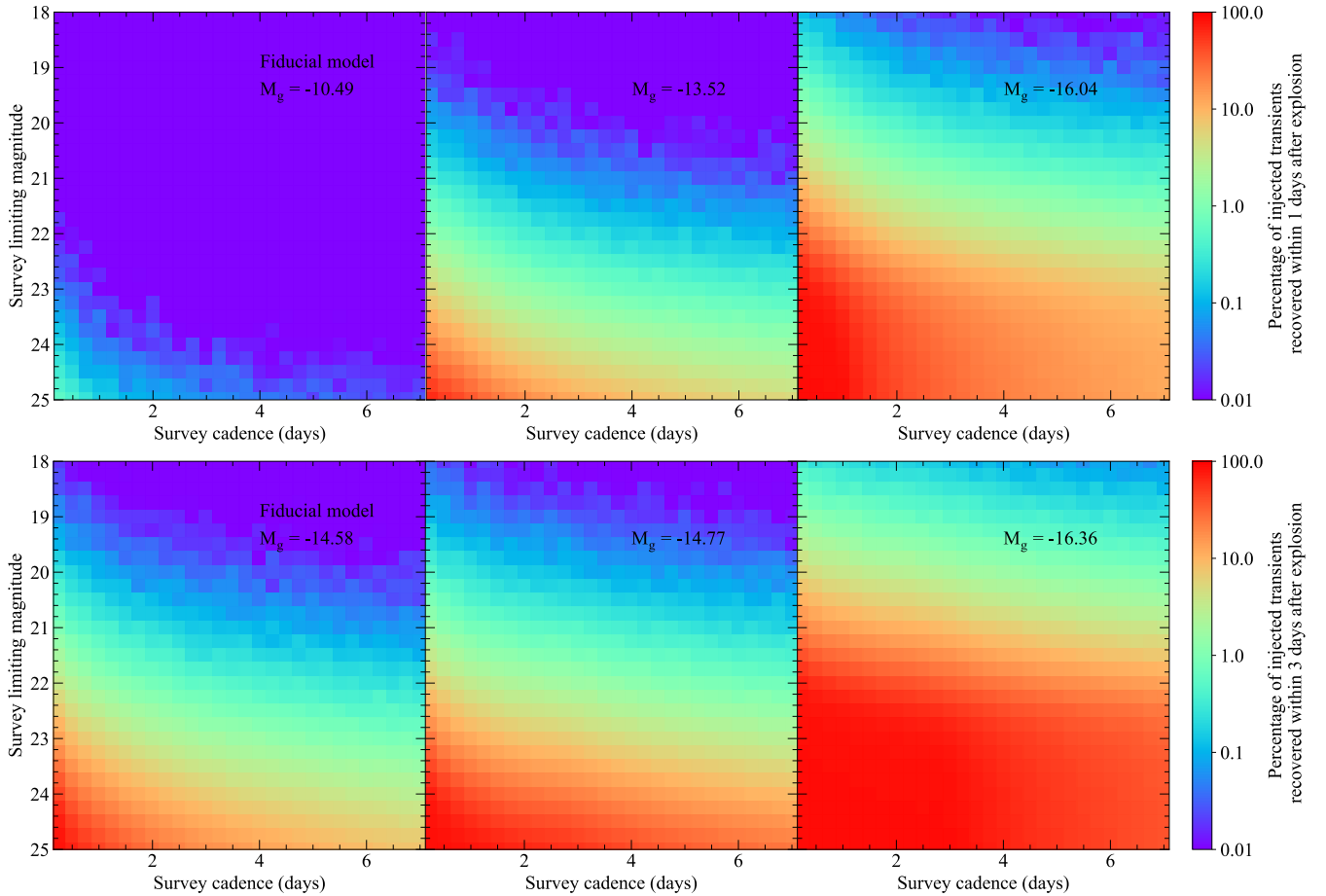


**Figure 5.** Percentage of injected transients recovered within one (top) and three (bottom) days of explosion for arbitrary survey depths and cadences. For each model, we give the absolute  $g$ -band magnitude at both times. We note that the colour-bar is shown on a log-scale.

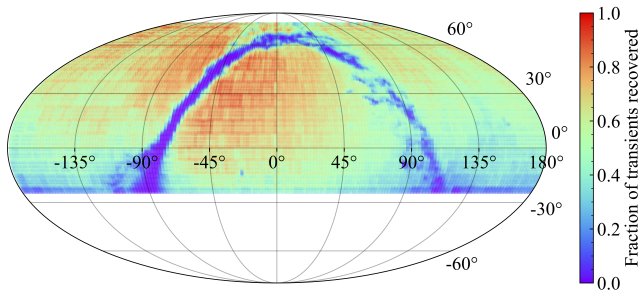


**Figure 6.** Recovery fraction for our ZTF I survey plan at different positions on the sky.

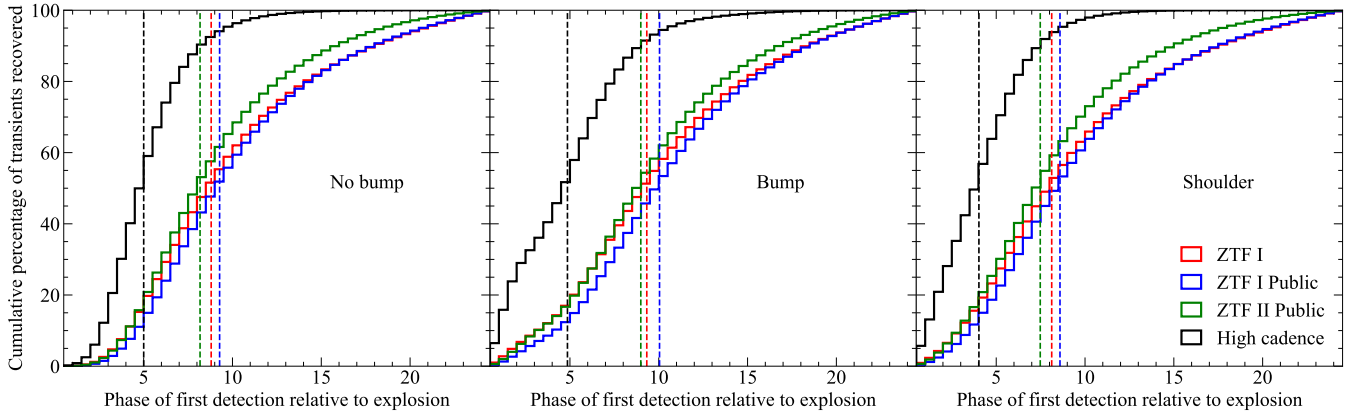
## 5.2 Phase of first detection

Figure 7 shows the cumulative distribution of rest-frame phases at which the injected transients are first detected at  $5\sigma$ . This is shown for each of our excess classifications (see Sect 2.2) and survey plans.

From Fig. 7, the median detection phase from the high cadence survey plan is 4 – 5 d after explosion depending on the early excess classification. Almost all first detections have been made by 7 – 9 d after explosion. For the no excess models,  $\lesssim 0.2\%$  (12%) of detections have been made by 1 d (3 d) after explosion. These results are comparable to our expectations based on the toy simulations shown in Fig. 5. Assuming a typical depth and cadence of 21 and 0.5 d, for

models without excesses 0 – 1% of the injected light curves should be recovered within  $\sim 1$  d of explosion, depending on their exact light curve shape (see Fig. 3). Likewise, 5.5 – 6.5% (32 – 35%) of first detections occur within 1 d (3 d) for the bump and shoulder models. Given the typical luminosities of the bump and shoulder models, our toy simulations indicate that 2 – 6% of the light curves are recovered within 1 d of explosion. This is again comparable to the prediction from our detailed ZTF simulation. Our toy simulations are therefore consistent with the more detailed ZTF simulations to within a factor of approximately a few. Discrepancies likely arise from differences in the specific light curve shapes of the models used in the ZTF simulations compared to the subset shown in Fig. 5.

The impact of an improved cadence is also demonstrated by the comparison between the first detection distributions of the ZTF I and II public simulations. For ZTF I public, the median phase of first detection is 8 – 10 d after explosion. In the ZTF II public survey the median detection phase is systematically lower by  $\sim 1$  d for each of the light curve types. The change from 3 d to 2 d cadence is therefore directly reflected in the phases of recovered transients. Given that the typical lifetimes of excesses are  $\lesssim 5$  d however, for both survey plans we would expect the majority of SNe Ia to show no signs of an excess, even if they all actually had one, as they are simply not observed early enough. Nevertheless, in ZTF I public,  $\sim 0.02\%$  (1.5%) of first detections for models without excesses occur within 1 d (3 d) of explosion, while 0.4 – 0.5% (5.6 – 7.3%) of first detections have occurred for models with an excess. In ZTF II public, this increases slightly to



**Figure 7.** Distribution of rest-frame first detection phase for each of our survey plans and early light curve classifications. Vertical dashed lines show the median detection phase for each survey plan.

$\sim 0.03\%$  (2.3%) for no excess and  $0.6 - 0.7\%$  (8.4 – 11.1%) for models with an excess. The improved cadence in ZTF II is therefore consistent with the prediction from our toy simulations that moving from a 3 d cadence to 2 d should result in  $\sim 50\%$  more young SNe Ia being discovered. Our simulations indicate that the ZTF high cadence survey could show up to approximately an order of magnitude increase in the number of young SNe Ia discovered relative to a 3 d cadence survey. While this is slightly higher than expected based on our toy simulations, the high cadence survey plan covered a smaller area and time-span and therefore is less affected by, for example, weather losses than the public surveys. We again note that the model light curves used in this study extend up to only a few days after maximum light. While the absolute number of transients recovered at early times will obviously not change, the relative proportion of these to the total number of recovered transients will. Therefore, given that the overall number of recovered transients is underestimated  $\lesssim 13\%$  (Sect. 5.1), these early recovery fractions should be considered to be upper limits with conservative relative uncertainties of 1 – 2%.

Although our simulations have focused on SNe Ia, these results, and the efficiencies shown in Fig. 5, should be broadly applicable to other SNe types. Given that the recovery efficiency of SNe Ia at 1 d after explosion is approximately  $20\times$  higher for those with an excess compared to those without, we would therefore expect that the majority of SNe Ia discovered at 1 d after explosion would contain an excess. This does however assume that SNe Ia with or without an excess are equally likely and the only limitation is our ability to detect sufficiently early. The fact that samples of young SNe Ia do not show such an overabundance of excesses indicates that they must instead be relatively rare. This point is discussed further in Sect. 6.2.

In Fig. 8 we show the distribution of non-detection phases for each of our survey plans. Here we define the non-detection phase as the time between the first  $5\sigma$  detection and previous non-detection. For the high cadence survey plan,  $\sim 75\%$  of recovered transients have a non-detection within 1 d of the first detection, while all transients have previous non-detections within  $\sim 5$  d. As it also includes observations of high cadence fields, the ZTF I survey plan shows a slightly higher fraction of non-detections within 1 d compared to both public plans, however the median phase of non-detection is  $\sim 3$  d. For ZTF I and II public, the difference in their median non-detection phases (3 d and 2 d, respectively) is again representative of the difference in cadence for the survey strategies. For ZTF I public,  $\sim 10\%$  of all recovered transients do not have a previous non-detection. In ZTF II

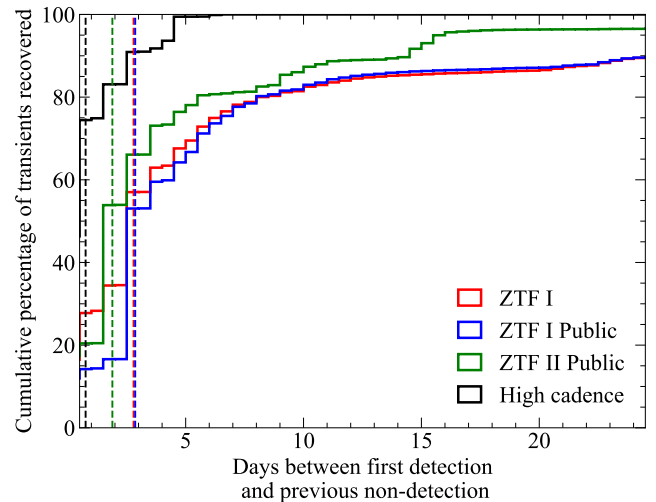


**Figure 8.** Distribution of the times between first detection and previous non-detection. Vertical dashed lines show the median for each survey plan.

public, this drops to  $\lesssim 4\%$ , however this may also be due to the shorter length of the survey simulated.

### 5.3 Early detections as a function of absolute magnitude

In Fig. 9 we show the impact of both absolute magnitude and redshift on the recovery statistics at different times for our ZTF I survey plan simulations. Figure 9 directly demonstrates the sensitivity of ZTF to early excesses at various redshifts. We separate all of the recovered transients into discrete, two-dimensional bins across redshift and absolute magnitude. Redshift bins are set to each encompass an equal volume, while the absolute magnitude bins contain an equal number of models. The absolute magnitudes are measured at 1 d and 3 d after explosion. With the magnitude and redshift bins defined, we calculate the fraction of recovered transients that were detected before each time within each bin. Figure 9 indicates the redshift at which each absolute magnitude would be observed with various signal-to-noise ratios. Similar plots for our ZTF I and II public, and high cadence survey plans are shown in Figs. A1, A2, and A3 respectively.

Within 1 d of explosion, many of the models without an excess



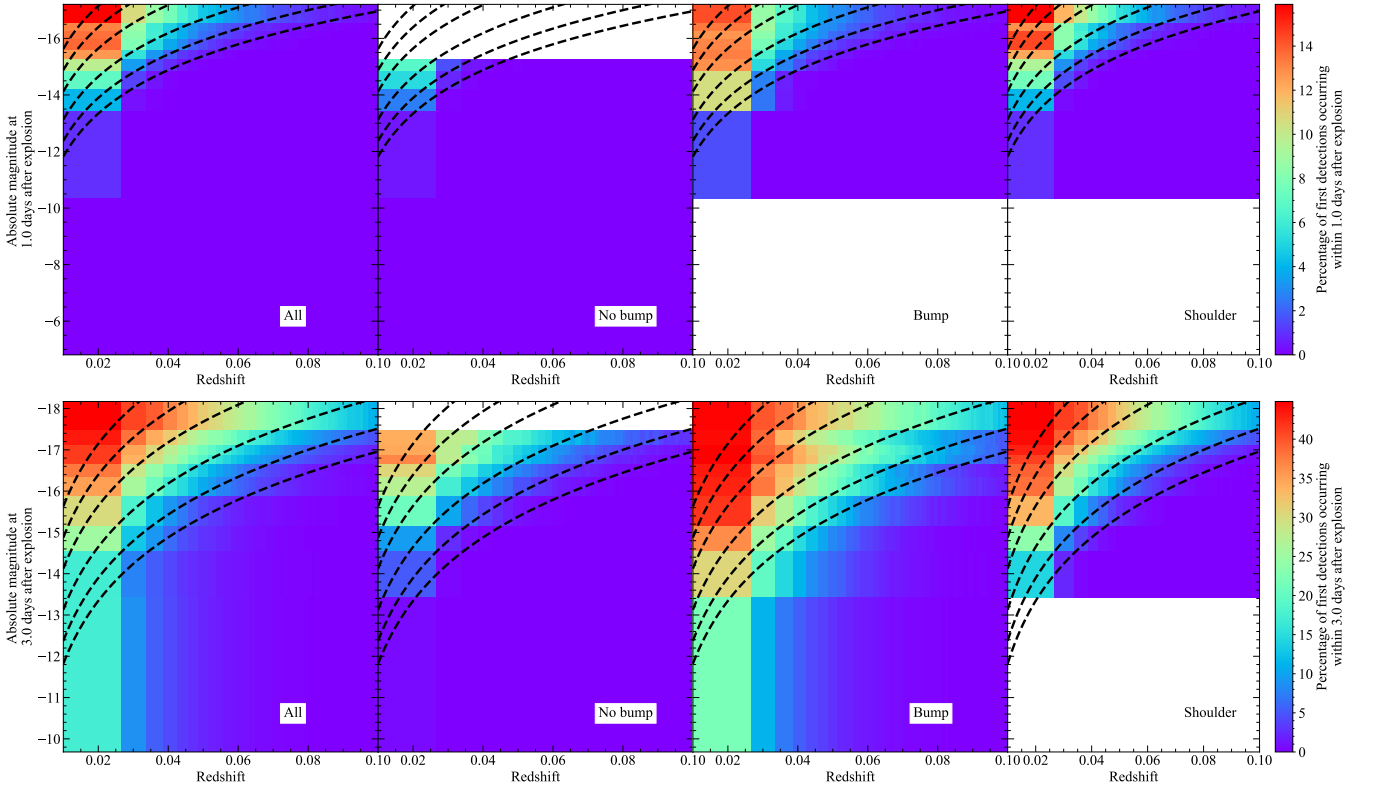


**Figure 9.** Fraction of recovered transients from the ZTF I survey plan detected before certain times as a function of absolute magnitude at that time and redshift. Times shown here are 1 d and 3 d post-explosion. In each row, we show the fraction for all transients and each of our early light curve classifications separately. We also note the different scales for colours in each row. Black dashed lines show the redshift at which a given absolute magnitude is observed with signal-to-noise ratios of 3, 5, 10, 25, 50, and 100. We note the different scales for the top and bottom panels.

are still experiencing the so-called dark phase (Piro & Nakar 2013), the time between explosion and the first light emerging from the SN. Hence, none of our models without bumps are brighter than approximately  $M_g = -15.3$ . In contrast, none of our models with early excesses are fainter than  $M_g = -10.3$ .

Figure 9 shows that the impact of the different early light curve behaviours on the recovery efficiencies is clearly apparent. The recovery efficiencies follow the expected trends, showing a greater proportion of early detections for SNe brighter at these phases and at low redshift. For example, within the first redshift bin ( $z \lesssim 0.027$ ), for transients brighter than  $M_g = -15.3$  at 1 d (i.e. those with an excess) 13 – 16% of recovered transients are first detected within 1 d of explosion. These SNe should be observed with high signal-to-noise ratios of  $\geq 10$ . These percentages steadily decrease out to higher redshifts and drop below  $\sim 1\%$  at  $z = 0.05$ , where the signal-to-noise ratio is  $\geq 3$ . For somewhat fainter models, those with an excess typically show higher recovery efficiencies than those without. In our first redshift bin, for models with  $-15 \lesssim M_g \lesssim -13.5$ , only 3 – 7% of detections occur within 1 d of explosion for models without an excess compared to 8 – 13% for models with a bump or shoulder. Although all models are binned here based on their absolute magnitudes at 1 d after explosion, the increased recovery efficiency of models with an excess is due to their overall faster rise during this time. Hence their average luminosity is higher for times  $\leq 1$  d after explosion compared to models without an excess, which are likely just exiting the dark phase. We also find that models with early excesses are observable to slightly higher redshifts compared to models without excesses within the same absolute magnitude bins.

For  $z \lesssim 0.05$ , 32 – 45% of all detections occur within 3 d of explosion for bright models (those that are brighter than  $M_g = -17.5$  at 3 d after explosion). Even out to the high redshift limit of our simulations,  $z = 0.1$ , as many as  $\sim 11\%$  of detections occur within 3 d of explosion for these models. At these redshifts, the signal-to-noise ratio is 5 – 10. In contrast, for the faintest magnitude bin ( $M_g \geq -13$ ) and lowest redshift bin, less than 1% of detections occur within 3 d of explosion for those models without an excess. The signal-to-noise ratio of these models is  $\leq 10$ . This percentage increases to  $\sim 22\%$  for models with bumps.

Comparing Figs. A1 & A2, we again show that a  $\sim 50\%$  increase in the number of young SNe Ia recovered should be expected for the higher cadence ZTF II public survey. For low redshift, bright SNe Ia, typically  $\sim 10\%$  (39%) of detections occur within 1 d (3 d) of explosion for models with an excess in the ZTF I public survey, while within ZTF II public this increases to  $\sim 16\%$  (55%). Similarly for the bright models without an excess at low redshift,  $\sim 4\%$  (28%) of detections should occur within 1 d (3 d) of explosion in ZTF I public, compared to  $\sim 6\%$  (42%) for ZTF II public.

## 5.4 Summary

Our simulations demonstrate the relative proportions of young SNe Ia that should be detected by ZTF and provide quantified recovery efficiencies to assess the likelihood of discovery. Of those transients recovered by our simulations, a significantly higher fraction of detections are made within the first few days of explosion for models with an excess compared to those without. Although the number of

young SNe Ia discovered by surveys is somewhat small, there is no such strong preference for those with excesses. This would indicate that flux excesses (at least those as bright as predicted by simulations) must be relatively rare. The comparison between our ZTF I and II public survey plans also shows that the improved cadence of ZTF II should produce a  $\sim 50\%$  increase in the number of young SNe discovered. Similarly, the ZTF high cadence survey should result in approximately up to an order of magnitude increase in the number of young SNe discovered. While the area of the high cadence survey is also approximately an order of magnitude smaller than the public surveys, the significantly improved temporal resolution should allow for the shapes of the early light curves to be better resolved and hence provide more meaningful constraints on the early excess. Although our simulations have focused on models of SNe Ia, we expect that this is also broadly applicable to other SNe types.

## 6 RATES

Given the recovery efficiencies described in Sect. 5, we can now place limits on the contribution of SNe Ia with excesses to the overall SNe Ia rate. We first verify the reliability of our simulations by applying our efficiencies to calculating the overall rate of SNe Ia.

### 6.1 Rate of SNe Ia

To calculate the rate of normal SNe Ia, we follow a similar method to that described by Frohmaier et al. (2019) for PTF, a precursor to ZTF. The rate of SNe Ia is defined as

$$r_V(z) = \frac{1}{V\Delta T} \sum_{i=1}^N \frac{1+z_i}{\epsilon_i}, \quad (2)$$

which counts the number of SNe Ia,  $N$ , that exploded within a given volume  $V$  and timespan  $\Delta T$ . Time dilation effects for each SN redshift are accounted for by the inclusion of the factor  $1+z_i$ . Each SN is also weighted by the recovery efficiency,  $\epsilon$ , which accounts for any similar SNe Ia that simply were not detected by the survey. The volume  $V$  is given by

$$V = \frac{\Theta}{41253} \frac{4\pi}{3} \left[ \frac{c}{H_0} \int_{z_1}^{z_2} \frac{dz}{\sqrt{\Omega_M(1+z)^3 + \Omega_\Lambda}} \right]^3 \text{Mpc}^3, \quad (3)$$

where  $z_1$  and  $z_2$  give the redshift boundaries over which the rate will be calculated and  $\Theta$  gives the survey area in  $\text{deg}^2$ . Here, we assume  $\Omega_M = 0.3$ ,  $\Omega_\Lambda = 0.7$ , and  $H_0 = 70 \text{ km s}^{-1} \text{ Mpc}^{-1}$ .

We use the sample of ZTF SNe Ia presented by Yao et al. (2019) to calculate the SNe Ia rate. This sample includes 127 SNe Ia observed during the partnership high cadence survey that were discovered at very early times (more than ten rest-frame days before  $B$ -band maximum) and therefore will form the basis for our estimates of the fraction of SNe Ia with excesses. As our simulations only include redshifts up to  $z = 0.1$ , we exclude higher redshift SNe from the following rate calculation, leaving a sample size of 90.

For the remaining SNe, we assign a weight based on the product of the recovery efficiency and spectroscopic completeness for the SN redshift. We determine the recovery efficiency by applying the same selection criteria used by Yao et al. (2019) (see their table 1) to our high cadence survey plan simulations calculated with the full Hsiao et al. (2007) template light curve. These selection criteria are therefore stricter than those used thus far (two  $5\sigma$  detections at any time), but as they are the same as what was applied to the observed sample they allow for a direct comparison between simulations and

observations. As part of their criteria Yao et al. (2019) also require that reference images for each SN are obtained earlier than 25 d before  $B$ -band maximum light. Approximately 81% of SNe meet this specific criterion. As our simulations do not include reference images, we assume a  $\sim 81\%$  likelihood that each SN would pass this selection cut and adjust the recovery efficiency accordingly. The spectroscopic completeness is given by Fremling et al. (2020) and Perley et al. (2020), who estimate that ZTF is  $\geq 95\%$  spectroscopically complete down to  $m_{\text{peak}} < 18.5$  and 75–89% complete at  $m_{\text{peak}} < 19$ . We convert this to a redshift dependence, assuming a typical absolute magnitude for SNe Ia of  $M_g = -19.2$ .

Summing over the 90 SNe Ia in the sample and appropriate weightings, as in Eqn. 2, we calculate a SN Ia rate for this sample of  $r_V = 2.56 \pm 0.24(\text{stat}) \pm 0.06(\text{sys}) \times 10^{-5} \text{ SNe yr}^{-1} \text{ Mpc}^{-3}$ . We estimate the statistical uncertainty as proportional to  $\sqrt{N}$ , where  $N = 90$ . Here the systematic uncertainty includes only the uncertainty resulting from spectroscopic completeness variations. For the PTF SNe Ia sample, Frohmaier et al. (2019) calculate a SN Ia rate of  $r_V = 2.43 \pm 0.29(\text{stat})^{+0.33}_{-0.19}(\text{sys}) \times 10^{-5} \text{ SNe yr}^{-1} \text{ Mpc}^{-3}$ . The agreement between both rates estimates demonstrates the reliability of our simulations and how the same selection criteria applied to our simulations results in a consistent SN Ia rate. We may therefore apply new cuts to both our simulations and the Yao et al. (2019) sample that will allow us to directly estimate the fraction of SNe Ia with an excess.

### 6.2 The intrinsic fraction of SNe Ia with an early excess

The agreement between the SNe Ia rates calculated using our simulations in Sect. 6.1 and literature values demonstrates the validity of these simulations. Given this, we now look to use `simsurvey` to constrain the fraction of SNe Ia that could have an early excess. If a large fraction of SNe Ia result from mechanisms that produce an excess, the number of SNe discovered shortly after explosion should be higher than if only a few SNe contain an excess. Therefore, given the sample of young SNe Ia from Yao et al. (2019),  $\mathcal{O}$ , we wish to calculate the most likely fraction of SNe Ia with an excess,  $\mathcal{R}_x$ , that reproduces the number of SNe discovered by ZTF in the sample. In other words the highest  $P(\mathcal{R}_x|\mathcal{O})$ .

To do this, we perform additional simulations whereby we vary the fraction of SNe Ia with an excess and count the number,  $\mathcal{N}$ , that meet the selection criteria used in Yao et al. (2019) and Sect. 6.1 at various time intervals. As we are interested in directly comparing the number of SNe Ia from our simulations to those observed, we use the rate calculated in Sect. 6.1 ( $2.56 \times 10^{-5} \text{ SNe yr}^{-1} \text{ Mpc}^{-3}$ ) rather than simply injecting a fixed number of 100 000 transients. We assume that  $\mathcal{R}_x$  is between 0–100% and repeat our simulations 10 000 times with the injected models randomly sampled for each iteration from those presented in Sect. 2. We apply the same cuts to our simulations as used in Yao et al. (2019) and Sect. 6.1. We further count the number of SNe passing these cuts that were observed between 0–1 d, 1–2 d, and 2–3 d after explosion, and between 3 d after explosion and maximum light. In focusing on the very early times in this way, we will be more sensitive to the number of SNe Ia with an excess. Figure 10 shows the distributions of the number of SNe Ia recovered across the 10 000 iterations for each  $\mathcal{R}_x$ . Unsurprisingly, Fig. 10 shows that as the fraction of SNe containing an excess increases, the number of discoveries at early times also increases. For example, if 100% of SNe Ia contained an excess, our simulations indicate that a median of  $\sim 22$  would be detected earlier than 1 d. In comparison, if 0% of SNe Ia contained an excess, only a median of  $\sim 2$  would be detected.

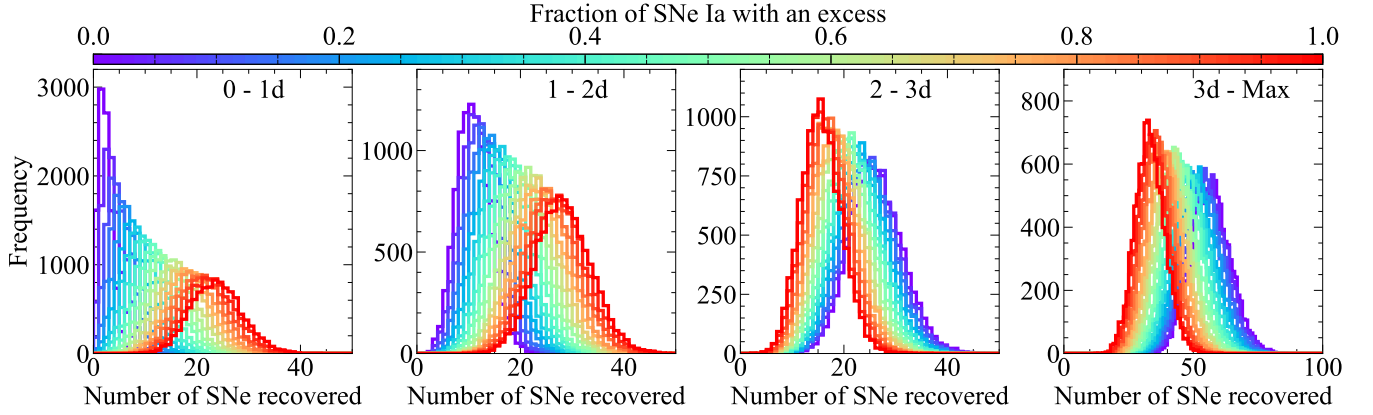


**Figure 10.** Number of SNe Ia recovered within various time bins, assuming a given fraction contain an excess at early times. For each fraction, we show the distribution in the number recovered across 10 000 survey simulations with randomly sampled input models.

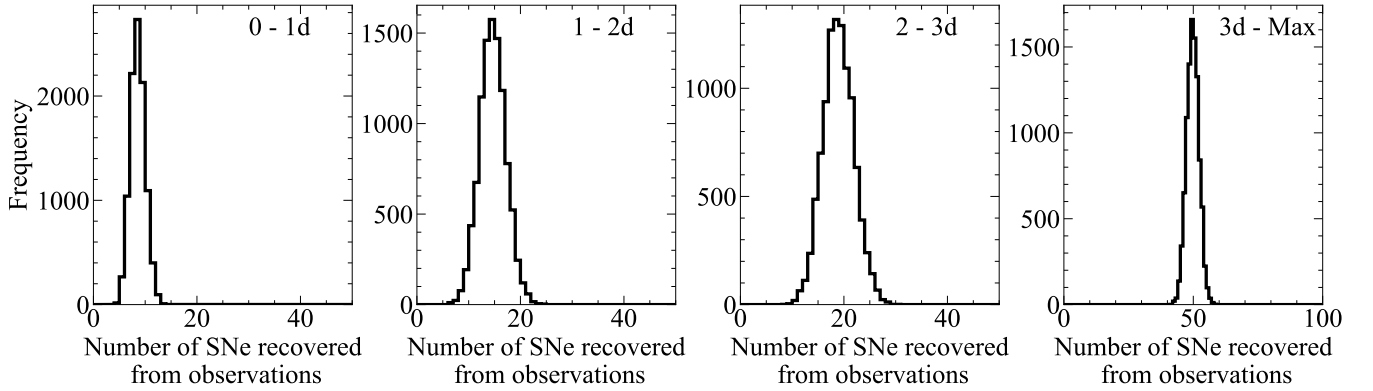


**Figure 11.** Number of SNe Ia recovered from ZTF within various time bins. The number of SNe Ia recovered in each bin is sensitive to the assumed explosion date, which is not known precisely. We perform 10 000 iterations whereby the explosion time of each SN is randomly sampled from the distributions found by Deckers et al. 2022. Each histogram shows the spread in the number of SNe recovered assuming these explosion times.

The distributions shown in Fig. 10 give the probability of detecting  $N$  SNe in each time bin, assuming some fraction,  $\mathcal{R}_x$ , of the intrinsic population contains an excess,  $P(N|\mathcal{R}_x)$ . From Bayes theorem,  $P(N|\mathcal{R}_x) \propto P(\mathcal{R}_x|N)$ . Hence, if  $N$  was exactly known from the observations, then to determine  $P(\mathcal{R}_x|O)$  we would simply need to count the number of simulations, out of 10 000, for which  $N$  SNe were detected. The explosion time of each SN however is not known precisely and therefore the number of SNe detected within a given bin will vary depending on the assumed explosion dates. To account for this we marginalise over the explosion times. By comparing to models from Magee et al. (2020), Deckers et al. (2022) estimated the explosion time for most SNe Ia in the Yao et al. (2019) sample. For 10 000 iterations, we randomly sample the probability distributions for the explosion time of each SN from Deckers et al. (2022) and calculate the number of SNe recovered within the time bins. These distributions are shown in Fig. 11 and hence provide the probability of detecting  $N$  SNe given the sample of observations  $O$ ,  $P(N|O)$ . The probability  $P(\mathcal{R}_x|O)$  is therefore given by the summation over all possible values of  $N$  and the product of individual probabilities within each time bin,  $j$

$$P(\mathcal{R}_x|O) \propto \prod_j \left( \sum_{N=0}^{\infty} P(N|O) P(N|\mathcal{R}_x) \right)_j. \quad (4)$$

The resultant probability distribution for the fraction of SNe Ia containing an excess is shown in Fig. 12.

From Fig. 12, we find  $\mathcal{R}_x \sim 28^{+13}_{-11}\%$ . With  $\geq 95\%$  confidence, we can exclude that  $\leq 7\%$  or  $\geq 55\%$  of SNe Ia contain an excess. Therefore, while some SNe Ia show signs of an excess, it is highly likely that most SNe Ia do not result from mechanisms that produce early excess emission. In addition, they could be somewhat common and account for approximately one in four SNe Ia.

## 7 DISCUSSION

### 7.1 Comparisons with previous estimates of the early excess rate

Comparing the recovered SNe Ia from our simulations to those recovered within ZTF, we estimate that the intrinsic rate of SNe Ia with an early excess is  $\sim 28^{+13}_{-11}\%$  of the overall population. We also exclude fractions of  $\leq 7\%$  or  $\geq 55\%$  at a 95% confidence level (Fig. 12).

Based on various samples of young SNe Ia, the fraction observed with an excess of flux at early times is estimated to range from 14 – 35%. Magee et al. (2020) present a series of radiative transfer models assuming different  $^{56}\text{Ni}$  distributions and demonstrate the strong impact this has on the luminosity at early times. Comparing these models to a sample of literature objects observed approximately

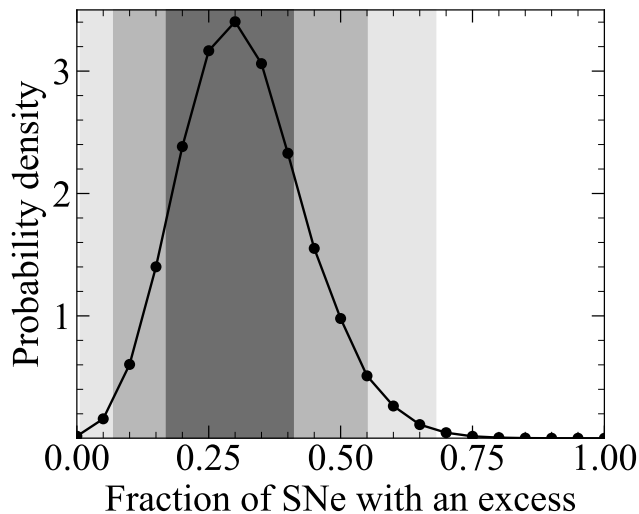


**Figure 12.** Probability density distribution for the fraction of SNe Ia containing an excess. Shaded regions show the 1, 2, and  $3\sigma$  range.

two weeks before maximum light, they estimate that  $\sim 22\%$  of the SNe Ia in their sample are inconsistent with their models and hence could show evidence for early excesses. Deckers et al. (2022) use the same method of model comparisons and compare to the sample of young ZTF SNe Ia from Yao et al. (2019) used in Sect. 6 for our rates calculations. They argue that  $\sim 18\%$  could show signs of an excess.

Rather than comparisons against model light curves, Jiang et al. (2018) use a visual classification scheme to estimate the early excess fraction. Here, early excesses are defined as either ‘spikes’, ‘bumps’, or generally having a broad light curve (relative to SN 2012cg). Jiang et al. (2018) estimate that  $\sim 35\%$  of the SNe in their gold sample can be classified as having an early excess. They also note however that the fraction of SNe Ia with an excess is highly dependent on the SN subclass. Finally, Jiang et al. (2020) present a handful of young SNe Ia observed as part of the HSC-SSP survey and estimate an early excess rate of  $\sim 14\%$  based on power-law fits to the early light curve.

The previously mentioned studies estimate the fraction of SNe Ia observed with an excess. As they are based on which SNe are observed, this may not be reflective of the intrinsic excess population. For example, SNe Ia with an excess are brighter at early times and hence could be over-represented in such samples. At the same time, if the explosion epoch is estimated to be later than the true value then the lack of an excess could simply be due to the fact that it has faded away by the beginning of observations and not that no excess was present. These cases would cause the excess fraction to be under-estimated. In contrast, our simulations and analysis naturally account for excess SNe Ia being brighter and uncertainty in the explosion epochs. We find that our estimate for the intrinsic rate of  $\sim 28_{-11}^{+13}\%$  is consistent with most estimates for the observed rate from the literature.

## 7.2 Implications for SNe Ia progenitors and explosion mechanisms

From our simulations of multiple different scenarios producing flux excesses at early times (such as double detonations,  $^{56}\text{Ni}$  clumps, and companion or CSM interaction), we find that overall such excesses are somewhat rare, but could account for approximately one in four SNe Ia. In spite of this, many of the individual mechanisms proposed

struggle in some way with reproducing the majority of the flux excess SNe Ia that have been observed to date.

Kasen (2010) estimate that, for all types of companion stars, the signature due to companion interaction would only be observable in  $\lesssim 10\%$  of cases. The observed number of young SNe Ia from Yao et al. (2019) is consistent with a population in which 10% contain an excess (within the 95% confidence region), however the companion interaction scenario struggles to reproduce many of the observed flux excesses. For example, the best fitting model presented by Hosseinzadeh et al. (2017) for the early light curve of SN 2017cbv over-predicts the UV flux. A similar issue is also observed by Miller et al. (2020) fitting the optical colours of SN 2019yvq. The disagreement between early light curves of this scenario and observations could result from some assumptions or missing physics, however companion interaction is also expected to produce late-time H or He emission, which has yet to be observed in early excess SNe Ia (e.g. Sand et al. 2018; Siebert et al. 2020).

Many of the observable signatures of companion interaction are similar to those produced by interaction with CSM, which has also been suggested for some SNe Ia with flux excesses. Here, the lack of strong H or He emission at late times could be explained if CSM was H- and He-deficient and instead dominated by other elements, such as C. This may be similar to what is required for some SNe Ia with excesses, however it also brings challenges if one attempts to explain the majority of the population. For example, Jiang et al. (2018) argue that 100% of the 91T-like SNe in their sample show evidence for early excesses. They argue that the short-lived C features seen in such SNe are inconsistent with a C/O-dominated CSM such as that produced by a merger. More models of interaction with H- and He-deficient CSM are required to fully understand the signatures that should be expected and hence the extent to which this scenario may or may not be excluded for some or all early excess SNe Ia.

Similarly, mechanisms producing red excesses, such as  $^{56}\text{Ni}$  clumps or double detonation explosions, are also likely ruled out as producing a significant fraction of SNe Ia with excesses. In these cases, while the decay of radioactive material near the surface of the ejecta can reproduce the shape of the excess, the colours produced around maximum light are significantly redder than normal SNe Ia, and indeed most early excess SNe Ia (e.g. Magee & Maguire 2020; Magee et al. 2021). Some red early excess SNe Ia do exist however, such as SN 2016jhr, which Jiang et al. (2017) argue is consistent with a double detonation explosion.

In summary, considering each of the different early excess scenarios used as part of this work, many of them produce similar observables (in terms of the excess luminosity and duration) and hence may be considered equally viable from our rate estimate. More detailed studies including colour and spectral evolution however have shown that this is not the case and therefore it is unlikely that any one of the scenarios considered here could fully explain the  $\sim 28_{-11}^{+13}\%$  of SNe Ia with an excess that is estimated from our simulations. Each of the scenarios may be relatively rare on their own, but given their similar light curve shapes at early times the combined effect overall could be that early excesses in general are more common.

## 8 CONCLUSIONS

In this work, we presented the first simulations specifically testing the recovery efficiency of young SNe Ia with and without an excess of flux. Such excesses have only been observed in a handful of cases, however it is unclear if this is because they are intrinsically rare or if this is due to the difficulty in observing SNe Ia sufficiently early.

Using `simsurvey`, we simulated four survey strategies, each based on observing logs from ZTF. As input for our simulations, we used existing radiative transfer models of SNe Ia from the literature. This set of models covers a broad range of early light curve luminosities and shapes, and includes models producing early excesses from companion interaction,  $^{56}\text{Ni}$  clumps, and helium shell detonations.

For each survey strategy, we ran multiple simulations with each of the different input models considered. Our simulations show that the typical recovery efficiency of the ZTF 3 d cadence public survey (where recovery is defined as having two  $5\sigma$  detections) is  $\sim 52\%$ . In this survey, we also find that only  $\lesssim 1.5\%$  of detections occur within the first 3 d following explosion for models without an excess. Models with an excess are of course more luminous at early times and therefore  $\sim 5.6 - 7.3\%$  of detections occur within the first 3 d. Since late 2020, the ZTF public survey has increased its observing cadence to 2 d and our simulations indicate that this should result in a  $\sim 50\%$  increase in the number of SNe Ia detections made during the first few days of explosion. Our simulations also show however, that if all SNe Ia did contain an excess,  $\lesssim 30\%$  would be detected early enough for this to be observed, even for a 2 d cadence survey.

From our survey simulations, we determine the recovery efficiency as a function of absolute magnitude and redshift. Using these recovery efficiencies we calculate the rate of SNe Ia within ZTF by applying the same selection criteria as Yao et al. (2019) and comparing to their sample of young SNe Ia. Using this SNe Ia rate, we perform additional simulations whereby we vary the fraction of SNe Ia that contain an excess. For each fraction, we calculate the number of young SNe Ia expected to be discovered within various time bins. By comparing to the number of SNe Ia in these same time bins from the Yao et al. (2019) sample, we find that  $\sim 28^{+13}_{-11}\%$  of SNe Ia could contain an excess, which is consistent with previous estimates from the literature.

The origin of early excesses in SNe Ia is unknown. Multiple scenarios have been proposed and, given the diversity in excesses observed, it is probable that multiple scenarios are required. While our simulations have constrained the excess rate to  $\sim 28^{+13}_{-11}\%$ , to place limits on the rate of each scenario is a challenging prospect and likely requires a larger sample of observed SNe Ia with excesses. Fortunately, the increased cadence of ZTF II will provide a significant increase in the number of young SNe Ia detected, which will prove invaluable for adding further constraints to the early excess origins.

## ACKNOWLEDGEMENTS

We thank the referee for their constructive comments, which helped to focus our manuscript. We thank T. Collett for useful discussions. MRM and KM are funded by the EU H2020 ERC grant no. 758638. This work has received funding from the European Research Council (ERC) under the European Union's Horizon 2020 research and innovation programme (LensEra: grant agreement No 945536). Based on observations obtained with the Samuel Oschin Telescope 48-inch and the 60-inch Telescope at the Palomar Observatory as part of the Zwicky Transient Facility project. Major funding has been provided by the U.S National Science Foundation under Grant No. AST-1440341 and by the ZTF partner institutions: the California Institute of Technology, the Oskar Klein Centre, the Weizmann Institute of Science, the University of Maryland, the University of Washington, Deutsches Elektronen-Synchrotron, the University of Wisconsin-Milwaukee, and the TANGO Program of the University System of Taiwan. M. W. C acknowledges support from the National Science Foundation with grant number PHY-2010970

## DATA AVAILABILITY

All models presented in this work are available on GitHub<sup>2</sup>.

## REFERENCES

- Almualla M., et al., 2021, *MNRAS*, 504, 2822  
 Andreoni I., et al., 2021, arXiv e-prints, p. arXiv:2104.06352  
 Bellm E. C., et al., 2019a, *PASP*, 131, 018002  
 Bellm E. C., et al., 2019b, *PASP*, 131, 068003  
 Brown P. J., Dawson K. S., Harris D. W., Olmstead M., Milne P., Roming P. W. A., 2012, *ApJ*, 749, 18  
 Cao Y., et al., 2015, *Nature*, 521, 328  
 De K., et al., 2019, *ApJ*, 873, L18  
 De K., et al., 2020, *ApJ*, 905, 58  
 Deckers M., et al., 2022, *MNRAS*,  
 Dekany R., et al., 2020, *PASP*, 132, 038001  
 Dimitriadis G., et al., 2019, *ApJ*, 870, L1  
 Feindt U., Nordin J., Rigault M., Brinnet V., Dhawan S., Goobar A., Kowalski M., 2019, *J. Cosmology Astropart. Phys.*, 2019, 005  
 Fremling C., et al., 2020, *ApJ*, 895, 32  
 Frohmaier C., et al., 2019, *MNRAS*, 486, 2308  
 Graham M. J., et al., 2019, *PASP*, 131, 078001  
 Hayden B. T., et al., 2010, *ApJ*, 722, 1691  
 Hoeflich P., Khokhlov A., 1996, *ApJ*, 457, 500  
 Höflich P., Khokhlov A., Wheeler J. C., Phillips M. M., Suntzeff N. B., Hamuy M., 1996, *ApJ*, 472, L81  
 Hosseinzadeh G., et al., 2017, *ApJ*, 845, L11  
 Hsiao E. Y., Conley A., Howell D. A., Sullivan M., Pritchett C. J., Carlberg R. G., Nugent P. E., Phillips M. M., 2007, *ApJ*, 663, 1187  
 Ivezić Z., et al., 2008, preprint, (arXiv:0805.2366)  
 Jha S. W., Maguire K., Sullivan M., 2019, *Nature Astronomy*, 3, 706  
 Jiang J.-A., et al., 2017, *Nature*, 550, 80  
 Jiang J.-a., Doi M., Maeda K., Shigeyama T., 2018, *ApJ*, 865, 149  
 Jiang J.-a., et al., 2020, *ApJ*, 892, 25  
 Kasen D., 2010, *ApJ*, 708, 1025  
 Kasliwal M. M., et al., 2020, *ApJ*, 905, 145  
 Kerzendorf W. E., Sim S. A., 2014, *MNRAS*, 440, 387  
 Kromer M., Sim S. A., Fink M., Röpke F. K., Seitenzahl I. R., Hillebrandt W., 2010, *ApJ*, 719, 1067  
 Kromer M., et al., 2016, *MNRAS*, 459, 4428  
 LSST Science Collaboration et al., 2009, preprint, (arXiv:0912.0201)  
 Liu Z.-W., Moriya T. J., Stancliffe R. J., 2015, *MNRAS*, 454, 1192  
 Livio M., Mazzali P., 2018, *Phys. Rep.*, 736, 1  
 Livne E., 1990, *ApJ*, 354, L53  
 Livne E., Glasner A. S., 1991, *ApJ*, 370, 272  
 Maeda K., Jiang J.-a., Shigeyama T., Doi M., 2018, *ApJ*, 861, 78  
 Magee M. R., Maguire K., 2020, *A&A*, 642, A189  
 Magee M. R., Sim S. A., Kotak R., Kerzendorf W. E., 2018, *A&A*, 614, A115  
 Magee M. R., Maguire K., Kotak R., Sim S. A., Gillanders J. H., Prentice S. J., Skillen K., 2020, *A&A*, 634, A37  
 Magee M. R., Maguire K., Kotak R., Sim S. A., 2021, *MNRAS*, 502, 3533  
 Masci F. J., et al., 2019, *PASP*, 131, 018003  
 Miller A. A., et al., 2020, *ApJ*, 898, 56  
 Ni Y. Q., et al., 2022, *Nature Astronomy*,  
 Noebauer U. M., Kromer M., Taubenberger S., Baklanov P., Blinnikov S., Sorokina E., Hillebrandt W., 2017, *MNRAS*, 472, 2787  
 Nugent P. E., et al., 2011, *Nature*, 480, 344  
 Olling R. P., et al., 2015, *Nature*, 521, 332  
 Perley D. A., et al., 2020, *ApJ*, 904, 35  
 Piro A. L., Morozova V. S., 2016, *ApJ*, 826, 96  
 Piro A. L., Nakar E., 2013, *ApJ*, 769, 67  
 Polin A., Nugent P., Kasen D., 2019, *ApJ*, 873, 84

<sup>2</sup> <https://github.com/MarkMageeAstro/TURTLs-Light-curves>

- Sagués Carracedo A., Bulla M., Feindt U., Goobar A., 2021, [MNRAS](#), **504**, 1294
- Sand D. J., et al., 2018, [ApJ](#), **863**, 24
- Scalzo R., et al., 2014, [MNRAS](#), **440**, 1498
- Schlegel D. J., Finkbeiner D. P., Davis M., 1998, [ApJ](#), **500**, 525
- Seitzzahl I. R., et al., 2016, [A&A](#), **592**, A57
- Shappee B. J., et al., 2014, [ApJ](#), **788**, 48
- Shappee B. J., et al., 2019, [ApJ](#), **870**, 13
- Shen K. J., Blondin S., Kasen D., Dessart L., Townsley D. M., Boos S., Hillier D. J., 2021, [ApJ](#), **909**, L18
- Siebert M. R., Dimitriadis G., Polin A., Foley R. J., 2020, arXiv e-prints, p. [arXiv:2007.13793](#)
- Soker N., 2019, arXiv e-prints, p. [arXiv:1912.01550](#)
- Tonry J. L., et al., 2018, [PASP](#), **130**, 064505
- Townsley D. M., Miles B. J., Shen K. J., Kasen D., 2019, [The Astrophysical Journal](#), **878**, L38
- Wang B., 2018, [Research in Astronomy and Astrophysics](#), **18**, 049
- Woosley S. E., Kasen D., 2011, [ApJ](#), **734**, 38
- Woosley S. E., Weaver T. A., 1994, [ApJ](#), **423**, 371
- Yao Y., et al., 2019, [ApJ](#), **886**, 152

## APPENDIX A: ADDITIONAL PLOTS

This paper has been typeset from a  $\text{\TeX/L\AA\TeX}$  file prepared by the author.

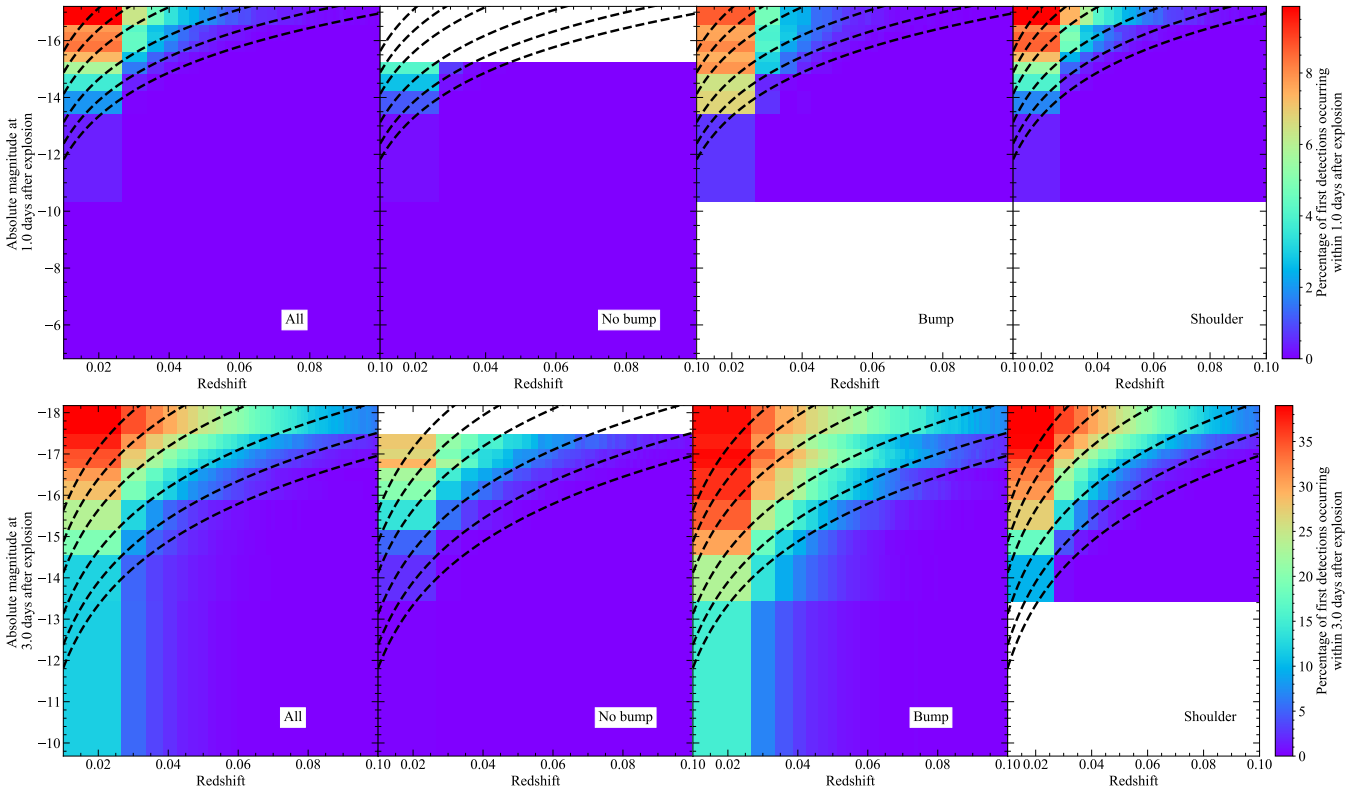


Figure A1. As in Fig. 9 for the ZTF I public survey plan.

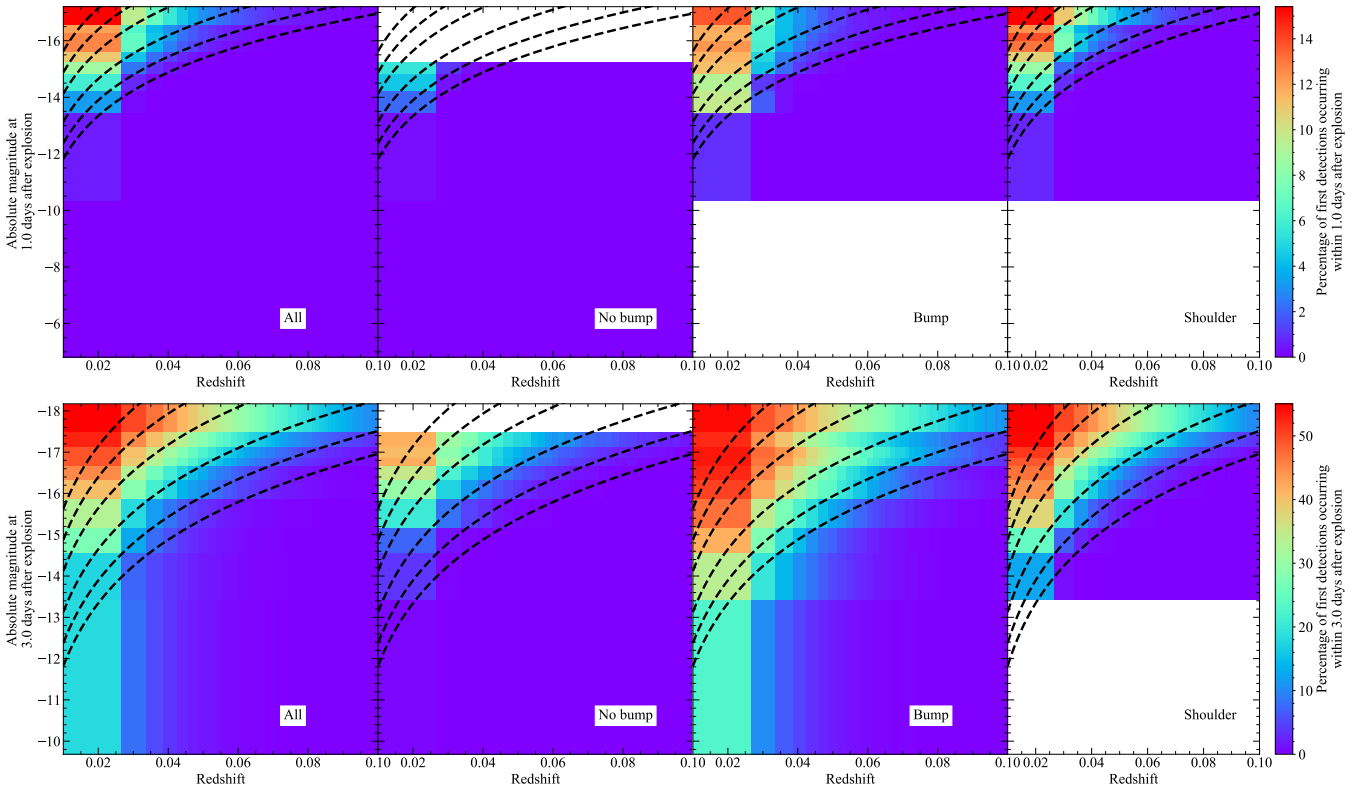
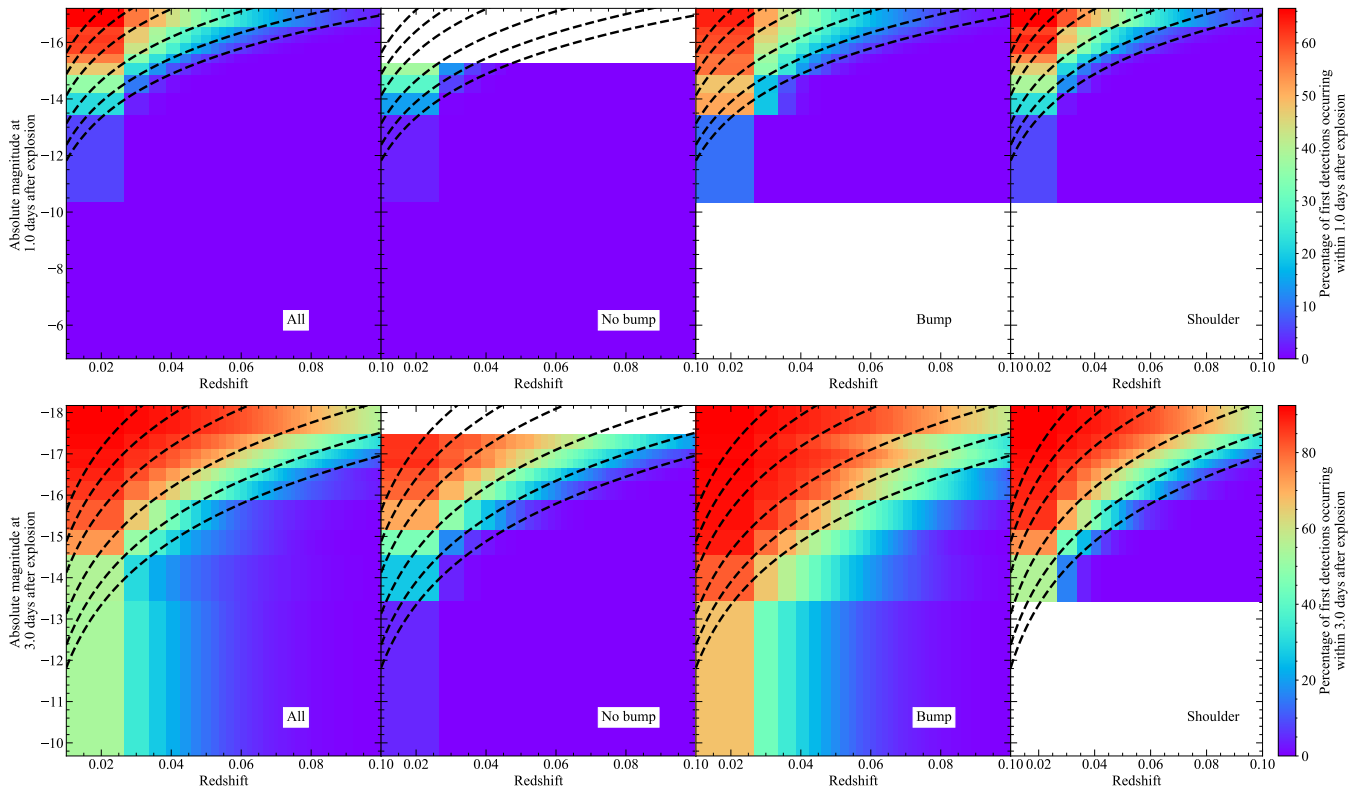


Figure A2. As in Fig. 9 for the ZTF II public survey plan.



**Figure A3.** As in Fig. 9 for the high cadence survey plan.